RSC Advances

ROYAL SOCIETY OF CHEMISTRY

www.rsc.org/advances

The Table of Contents entry

Graphic:

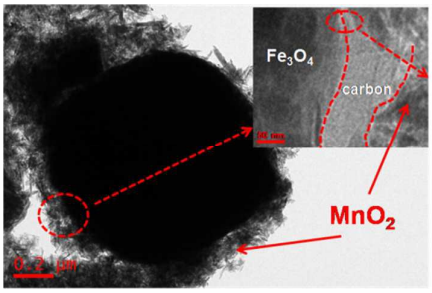

Text:

Fe_3O_4@(C-MnO_2) composite with a cube-like core-double-shell structure as an anode material has been successfully prepared.

Fe_3O_4@(C-MnO_2) Core-double-shell Composite as High-Performance Anode Material for Lithium Ion Batteries

Yanqing Fu, Xianyou Wang*, Hao Wang, Youwei Zhang, Xiukang Yang, Hongbo Shu*

(Key Laboratory of Environmentally Friendly Chemistry and Applications of Ministry of Education，Hunan Province Key Laboratory of Electrochemical Energy Storage and Conversion，School of Chemistry, Xiangtan University, Hunan, Xiangtan 411105, China)

Abstract: The Fe_3O_4@(C-MnO_2) composite with a cube-like core-double-shell structure has been successfully designed and prepared by a combination of the hydrothermal method and layer-by-layer (LBL) self-assembly technique. This novel hybrid composite was characterized by X-ray powder diffraction (XRD), scanning electron microscopy (SEM), transmission electron microscopy (TEM), energy dispersive X-ray (EDX) spectroscopy and electrochemical tests. It has been found that this material is the cube-like morphology with core-double-shell structure. Compared with the bare α-Fe_2O_3 and Fe_3O_4-C materials, the as-prepared composite as an anode material for lithium ion batteries (LIBs) exhibits significantly enhanced electrochemical performance with a high capacity, good rate capability, and excellent cycling stability. At a current density of 100 mA g^{-1}, the as-obtained Fe_3O_4@(C-MnO_2) composite electrode delivers a reversible capacity exceeding 1000 mA h g^{-1} and retains 979 mA h g^{-1} after 150 cycles. In contrast, the discharge capacities of the bare α-Fe_2O_3 and Fe_3O_4-C show only 111 mA h g^{-1} and 282 mA h g^{-1} at the current density of 100 mA g^{-1} after 150 cycles, respectively. This improved electrochemical performance can be attributed to high theoretical capacity and larger specific surface

* **Corresponding author:** Xianyou Wang Tel: +86 731 58292060; fax: +86 731 58292061.
E-mail address: wxianyou@yahoo.com (X. Wang), hongboshuxtu@gmail.com.

of the MnO_2 layer, as well as the high electrical conductivity of carbon layer which acts as both the linker and the stabilizer between Fe_3O_4 and MnO_2.

Keywords: Lithium ion batteries; Anode material; Electrochemical performance; Ferriferrous oxide; Core-double-shell structure

1. Introduction

In recent years, it has aroused a great deal of interest in seeking for high-performance electrode materials with the capability to store and deliver energy efficiently for lithium ion batteries (LIBs).[1-4] In terms of the anode materials, traditional graphite is widely used in commercial LIBs because of their low cost and long cycle life. However, low theoretical capacity (372 mA h g^{-1}) limits its widespread application in high performance LIBs. Compared with carbon-based materials, transition metal oxides (TMOs) with a novel conversion mechanism which could offer high theoretical specific capacity (~1000 mA h g^{-1}) are supposed to be one of the most promising anode materials, such as α-Fe_2O_3,[5] MnO_2,[6] Co_3O_4,[7] NiO,[8] Fe_3O_4,[9] and so forth. Among all TMOs, iron oxide has attracted much attention owing to its low toxicity, plentiful raw materials, high corrosion resistance, improved safety and low processing cost.[10-12] Nevertheless, the poor cycling stability and low rate capability which caused by the large specific volume changes during charge/discharge cycling process and kinetic limitations of its intrinsic nature, still strongly restrict its large-scale practical application.

To solve the thorny problem, surface modification has been proved an effective

way. It has been reported that carbon coating is the most widely used technique to increase the electronic conductivity of electrode materials and maintain the integrity of particles.[10, 12, 13] Zhang et al.[14] synthesized Fe_3O_4/C nanospindle as anode material by hydrothermal treatment of α-Fe_2O_3 precursors with glucose, it showed high reversible capacity with 745 mA h g^{-1} at the current density of 185 mA g^{-1}. In addition, Xiong et al.[15] fabricated porous Fe_3O_4/C core-double-shell nanorods through partial reduction of porous α-Fe_2O_3 particles with carbon coating and obtianed specific capacity of 762 mA h g^{-1} at 92.4 mA g^{-1} after 50 cycles. Liu et al.[16] prepared Fe_3O_4/C composites with specific capacity of 488 mA h g^{-1} at 60 mA g^{-1}. However, as the buffer for mitigating the volume change during cycling, carbon on one side of the active materials didn't maximize its exertion, leading to the limited capacity of electrodes. To resolve this drawback, assembly of different oxides into a hierarchical composite is a good solution and a research hotspot, which could take full advantages of different components for the better performance in LIBs.[17,18] Very recently, another environmental friendly and resourceful compound manganese dioxide (MnO_2), with high theoretical capacity and relatively low electrochemical motivation force, has attracted great attention due to their wide applications in catalysis and energy storage.[19-21] Notably, it has been reported that loading nanostructured MnO_2 onto a conductive layer by layer-by-layer (LBL) deposition can achieve high reversible capacities as anode materials for LIBs.[22, 23]

Herein, the Fe_3O_4@(C-MnO_2) core-double-shell composite with cube-like morphology was successfully designed and synthesized by a mild hydrothermal

reaction and the LBL technique. Specifically, Fe_3O_4-C particle was first prepared via partial reduction of α-Fe_2O_3 cube with carbon coating and then MnO_2 nanomaterials were deposited on the surface of Fe_3O_4-C by combining the *in situ* chemical redox reaction between the carbon layer and $KMnO_4$ to form the Fe_3O_4@(C-MnO_2) composite, as illustrated in Scheme 1. To the best of our knowledge, such a novel core-double-shell Fe_3O_4@(C-MnO_2) composite, which is found showing much better electrochemical properties including high specific capacity and improved cycling performance, has rarely been reported. Moreover, the physicochemical and electrochemical properties of the as-prepared Fe_3O_4@(C-MnO_2) composite are studied in detail.

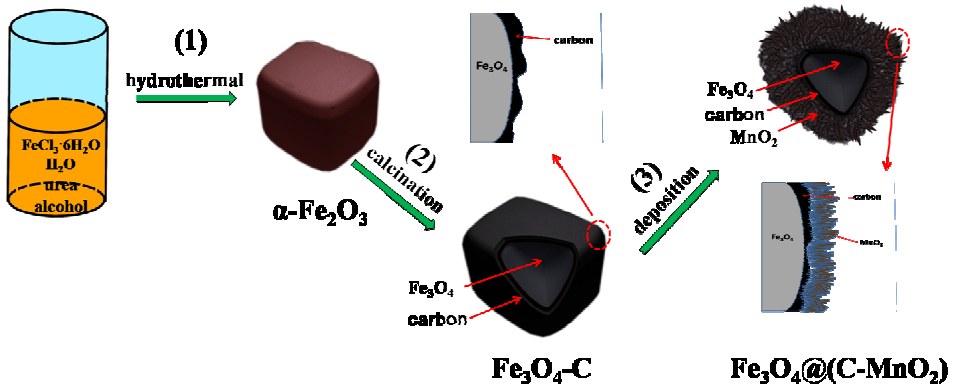

Scheme 1 Schematic illustration of the synthetic process of the cube-like Fe_3O_4@(C-MnO_2) core-double-shell composite.

2. Experimental

2.1 Synthesis of α-Fe_2O_3 cubes

All the reactants below were of analytical grade and used without further purification. In a typical synthesis, 30 mL deionized water and 30 mL absolute

ethanol were mixed together, then 1.3 g (4.8 mmol) $FeCl_3 \cdot 6H_2O$ and 0.3 g (5.0 mmol) urea were added to the solution. After stirring to form a homogeneous solution, the mixture was transferred into a 100 mL Teflon autoclave and then reacted at 180 °C for 6 h in an oven. After cooling down to room temperature, the precipitate was collected by centrifugation and then washed with deionized water and absolute ethanol for several times respectively, followed by dried at 70 °C for 12 h in an oven. Finally, the desiccated sample was heated in a quartz tube to 400 °C in air at a rate of 5 °C min^{-1} and kept at this temperature for 3 h to obtain reddish-brown α-Fe_2O_3 submicron cube.

2.2 Synthesis of Fe_3O_4-C particles

A 0.6 g as-prepared hematite particles was mixed with a certain amount of solid citric acid in ethanol by grinding gently, the powder was then obtained after the evaporation of ethanol. Finally, the desiccated sample was carbonized at 600 °C for 4 h in N_2 atmosphere at a rate of 5 °C min^{-1} to obtain black Fe_3O_4-C particles.

2.3 Synthesis of Fe_3O_4@(C-MnO_2) particles

0.3 g of as-prepared carbon coated Fe_3O_4 particles was dispersed in 75 mL of 0.03 M $KMnO_4$ aqueous solution under high-power ultrasonication for 1 h. Then, the suspension was transferred into a 100 ml Teflon autoclave and maintained at 180 °C for 6 h in an oven. After cooling down to room temperature, the chocolate-color product was collected by centrifugation and washed with deionized water and absolute ethanol several times respectively, followed by dried at 120 °C for 12 h in an oven.

2.4 Physical characterizations

The phase purity and structure of the as-synthesized samples was characterized by X-ray powder diffraction (XRD) using a Rigaku D/MAX-2500 powder diffractometer with a graphite monochromatic and Cu Kα radiation (λ = 0.15418 nm) operated at a scan rate of 2° min^{-1} in the 2θ range of 10°-80°, with a step size of 0.01°. Scanning electron microscopy (SEM) images were collected using a JEOL JSM-6610 scanning electron microscope. Transmission electron microscopy (TEM) and high-resolution transmission electron microscopy (HRTEM) observations, as well as energy dispersive X-ray (EDX) spectroscopy analyses were obtained using a JEOL JEM-2100F transmission electron microscope at an acceleration voltage of 200 kV. The specific surface area and pore size distribution curves of the samples were determined by N_2 adsorption/desorption isotherm at 77 K (JW-BK112). The chemical composition of as-synthesized sample was detected by atomic absorption spectroscopy (AAS, Vario 6 Analytik Jena AG, Jena). The thermogravimetric analysis (TGA) was carried out by TGA Q50 V20.8 Build 34.

2.5 Electrochemical Measurements

The electrochemical tests of the as-prepared samples were carried out using two-electrode button-type cells assembled in an argon-filled glove box, where water and oxygen concentration were kept less than 5 ppm. The working electrodes were fabricated by mixing 70 wt% of active materials, 20 wt% of acetylene black and 10 wt% of polymer binder (polyvinylidene fluoride, PVDF), which were then pasted on copper foil followed by drying under vacuum at 110 °C for 10 h. Lithium disc was served as both counter electrode and reference electrode. 1 M $LiPF_6$ in a mixture of

ethylene carbonate (EC) and edimethyl carbonate (DMC) (1:1, V/V) was used as an electrolyte and the separator was a Celgard 2400. The galvanostatic charge-discharge measurements were performed using a Neware battery tester BTS-XWJ-6.44S-00052 (Neware, Shenzhen, China) at different current densities with a cut-off voltage window of 0.01-3.0 V. The calculation of the specific capacity is based on the overall mass of the composite synthesized. Cyclic Voltammetry (CV) tests were carried out on VersaSTAT3 electrochemical workstation (Princeton, America) at a scan rate of 0.1 mV s^{-1} with the potential interval 0.01-3.0 V (vs. Li^+/Li). Electrochemical impedance spectroscopy (EIS) was also performed using VersaSTAT3 electrochemical workstation by applying an ac amplitude of 5 mV over the frequency range from 10^5 to 0.1 Hz. All the electrochemical measurements were performed at room temperature.

3. Results and discussion

3.1 Structural and morphology analysis

X-ray diffraction (XRD) analysis is used to determine the phase structure of the samples. Fig. 1a is the XRD pattern of the as-prepared α-Fe_2O_3, in which all the diffraction peaks are in good agreement with the standard hematite (α-Fe_2O_3) crystal structure (JCPDS No. 33-0664), indicating that a pure and highly crystalline product has been obtained. After coating a carbon layer, the XRD pattern of Fe_3O_4-C sample is shown in Fig. 1b. All peaks indicated by Miller indices in the pattern can be well indexed to the face-centered Fe_3O_4 (JCPDS No. 74-0748), which demonstrates that

the pure α-Fe_2O_3 was converted to Fe_3O_4.[11, 14] Besides, there are no other diffraction peaks can be obviously observed, suggesting an amorphous carbon. The diffraction peaks of MnO_2 modified Fe_3O_4-C particle (Fig. 1c), have more different positions from Fe_3O_4-C after the LBL technique involving the deposition of MnO_2, which are well confirmed to the peaks of MnO_2 (JCPDS No. 44-0141), indicating that MnO_2 exists in the Fe_3O_4@(C-MnO_2) sample.

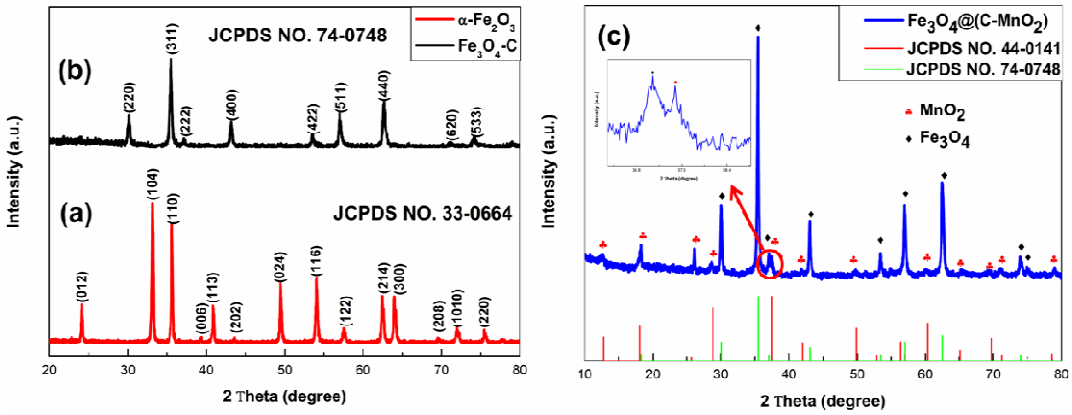

Fig. 1 XRD patterns of (a) α-Fe_2O_3, (b) Fe_3O_4-C and (c) Fe_3O_4@(C-MnO_2).

Typical scanning electron microscopy (SEM) images are applied to understand the morphologies and microstructures of the as-obtained samples as shown in Fig. 2. It is quite clear that the structure of α-Fe_2O_3 precursor is cubic with size of 400~800 nm and the color is reddish-brown (inset in Fig. 2a). After sintering the mixture of α-Fe_2O_3 particle with citric acid, as displayed in Fig. 2b, the morphology of Fe_3O_4-C is perfectly retained as cube-like structure without noticeable variation compared with that of α-Fe_2O_3 precursor, except that the outer surface becomes coarse and its color converts to black (inset in Fig. 2b), indicating that carbon coats on the surface of Fe_3O_4 particles. After a mild hydrothermal reaction between $KMnO_4$ and Fe_3O_4-C cube, as shown in Fig. 2c, Fe_3O_4@(C-MnO_2) still maintains the cubic morphology,

but reveals more rough surface than Fe_3O_4-C. Moreover, the color of the sample changes into chocolate-color (inset in Fig. 2c). It indicates that MnO_2 is probably introduced.

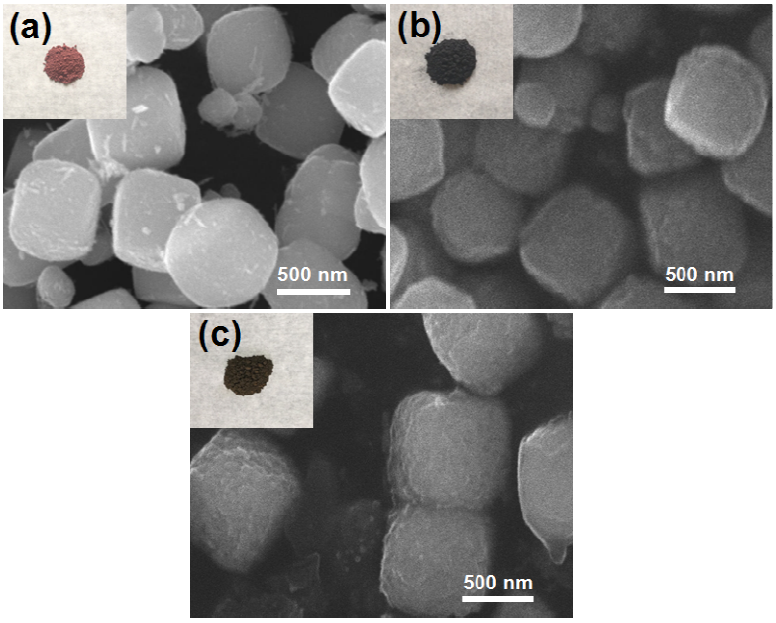

Fig. 2 SEM and optical images (insets) of (a) α-Fe_2O_3, (b) Fe_3O_4-C and (c) Fe_3O_4@(C-MnO_2).

To further insight into the morphology and structure of the samples, transmission electron microscopy (TEM) and high-resolution transmission electron microscopy (HRTEM) observations were carried out. Fig. 3a and b show the morphology of precursor is cubic and the lattice spacing of 0.37 nm can be assigned to the (012) plane of α-Fe_2O_3, which are well consistent with SEM and XRD, respectively. The TEM image in Fig. 3d displays the cube-like α-Fe_2O_3 is coated with carbon. Further information can be learned from Fig. 3e, it is quite clear that the amorphous carbon layer is located around the surface and the lattice fringes with spacings of 0.48 nm and 0.25 nm are attributed to the (111) and (311) planes of face-centered Fe_3O_4, respectively, revealing α-Fe_2O_3 is converted to Fe_3O_4 after calcining. This is well

184 consistent with the XRD pattern of Fe_3O_4-C. The Fe_3O_4-C particles can be
185 encapsulated by amorphous MnO_2 layer which is produced by chemical redox
186 reaction between the carbon layer and $KMnO_4$ based on the following reaction.

187 $$4KMnO_4 + 3C + H_2O = 4MnO_2 + 2KHCO_3 + K_2CO_3 \quad (1)$$

188 Thus, a rough surface with some needle-like and flocculus-like nanomaterials is
189 observed as shown in Fig. 3g, resulting in a higher surface area. The inset of Fig. 3g is
190 from the partial area of the TEM image (the red circle in Fig. 3g), which is magnified
191 to confirm needle-like MnO_2 layer deposited on the surface of carbon layer. From it,
192 the carbon and MnO_2 layers are clearly seen. Furthermore, from the HRTEM as
193 displayed in Fig. 3h, the lattice fringes with interplanar spacings of 0.21 nm, 0.19 nm
194 and 0.24 nm are in good accordance with the (301), (510) and (211) planes of MnO_2
195 (JCPDS No. 44-0141), respectively. This result is well consistent with XRD data.
196 Obviously, the middle layer is amorphous carbon in Fig. 3h. On the other side of
197 carbon, the lattice fringe of 0.29 nm is observed, corresponding to the planes of
198 face-centered Fe_3O_4. From Fig. 3g and h, it can be seen that the Fe_3O_4@(C-MnO_2)
199 core-double-shell composite with cube-like morphology is successfully prepared.

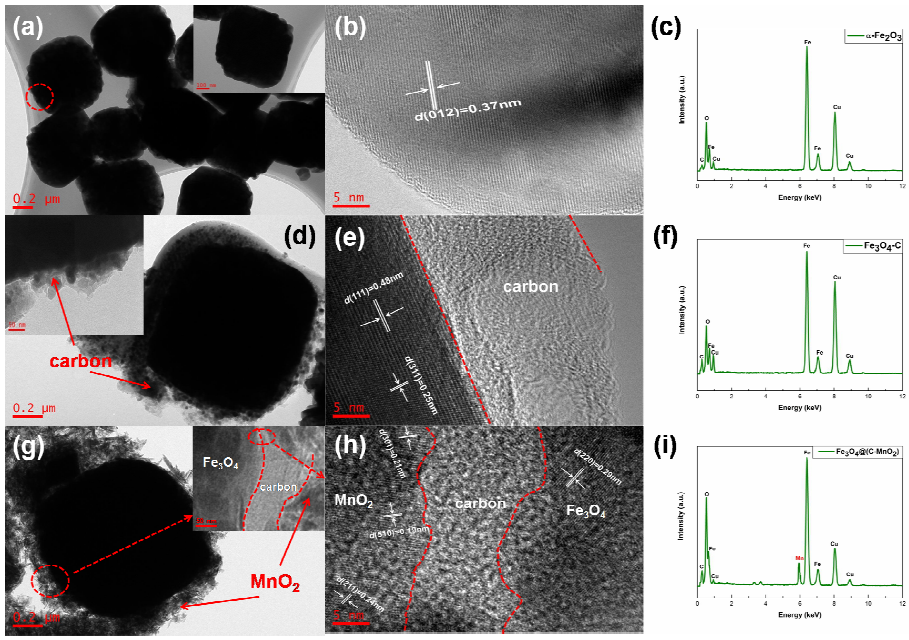

Fig. 3 TEM images, HRTEM images and EDX spectrums of (a, b and c) α-Fe_2O_3, (d, e and f) Fe_3O_4-C and (g, h and i) Fe_3O_4@(C-MnO_2).

The energy-dispersive X-ray (EDX) analysis is used to further verify the elements of the samples. Except Cu (the Cu peaks in all the spectrums come from the copper substrates), it can be observed from Fig. 3 (c, f and i) that the Fe, O and C elements exist in both Fe_3O_4-C and Fe_3O_4@(C-MnO_2) samples (Fig. 3f and i), indicating the presence of carbon. It should be noted that there is also C element presented in Fig. 3c, but the C peak intensity is apparently lower than Fe_3O_4-C and Fe_3O_4@(C-MnO_2) samples, which may be put down to the use of TEM grid (containing C element) in the test. Particularly, Fig. 3i reveals the final product is composed of Fe, O, C and Mn elements. Remarkably, the weak peaks placed at 3.5-4.0 keV are likely to be from the $KHCO_3$ and/or K_2CO_3 during the redox deposition of MnO_2.[23]

Nitrogen adsorption-desorption measurements were carried out at 77 K to study

the textural characteristics of these three samples. Fig. 4c shows nitrogen-sorption data of Fe_3O_4@(C-MnO_2), revealing a Brunauer-Emmett-Teller (BET) surface area of 32.50 m^2 g^{-1}, which is much higher than that of α-Fe_2O_3 (8.66 m^2 g^{-1}, Fig. 4a) and Fe_3O_4-C (10.89 m^2 g^{-1}, Fig. 4b). The pore size distributions (insets) of all three samples are derived from the adsorption branch of isotherms based on the Barrette-Joynere-Halenda (BJH) model. They are mainly in the range of 1.5-5 nm, and the mean pore diameters are 2.87, 2.86 and 2.65 nm, respectively.

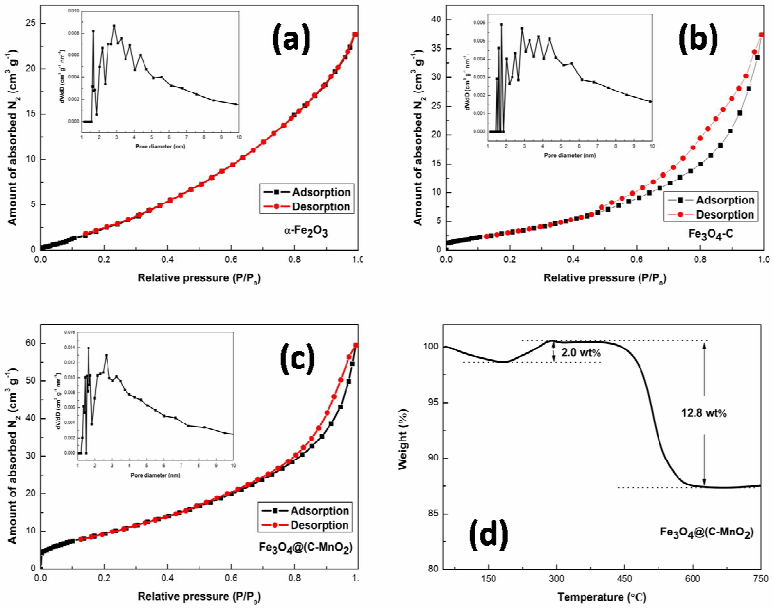

Fig. 4 Nitrogen adsorption-desorption isotherms and pore size distribution curves (insets) based on the BJH method of (a) α-Fe_2O_3, (b) Fe_3O_4-C and (c) Fe_3O_4@(C-MnO_2); (d) the TGA result of Fe_3O_4@(C-MnO_2), and the profile was taken in air with a heating rate of 5 °C min^{-1}.

Thermogravimetric analysis (TGA) was carried out in air at a heating rate of 5 °C min^{-1} to analyze the carbon content in Fe_3O_4@(C-MnO_2). In Fig. 4d, because of removal of the weakly adsorbed water and other small volatile molecules, the TGA curve displays a first weight loss from 50 °C to 200 °C. Then a following weight gain

(~2.0 wt%) corresponds to the transformation of Fe_3O_4 to Fe_2O_3. The second weight loss at higher temperature could be mainly attributed to the evaporation and subsequent decomposition of the amorphous carbon layer. Therefore, there is ~12.8 wt% carbon in Fe_3O_4@(C-MnO_2) from the TGA. Furthermore, according to the atomic absorption spectroscopy (AAS), the Fe_3O_4@(C-MnO_2) composite is detected with 61.5 wt% Fe_3O_4 and 26.0 wt% MnO_2. As a result, the theoretical capacity of Fe_3O_4@(C-MnO_2) is about 935.1 mA h g^{-1} (935.1 mA h g^{-1} = 924 mA h g^{-1} × 61.5 wt% + 372 mA h g^{-1} × 12.5 wt% + 1232 mA h g^{-1} × 26 wt%).

3.2 Electrochemical Analysis

Fig. 4(a, c and e) show the typical cyclic voltammetric (CV) curves for α-Fe_2O_3, Fe_3O_4-C and Fe_3O_4-C@MnO_2 electrodes between 0.01 and 3 V at a scan rate of 0.1 mV s^{-1}. With regard to Fig. 4a and c, the cathodic current peaks positioned at 0.58 V and 0.51 V in the first cycle can respectively be ascribed to a reversible conversion reaction of α-Fe_2O_3 and Fe_3O_4 with the metallic lithium to form lithia (Li_2O) and metallic iron (Fe^0), as well as the electrolyte decomposition to form SEI films.[24, 25] In addition, in the anodic processes, two peaks are presented at 1.65 V and 1.66 V, corresponding to the reversible oxidation process of Fe^0 to Fe^{3+}.[26] Apparently, the peak intensities of the two samples drop dramatically in the second cycles, indicating the occurrence of some irreversible processes in the first cycling process, which can be attributed to the formation of SEI film and electrolyte decomposition. Furthermore, the intensities of 30th and 50th curves are obviously reduced, thus resulting in an inferior capacity. For the Fe_3O_4@(C-MnO_2) electrode (Fig. 4e), in the first cycle, the

fairly sharp cathodic current peak is located at about 0.20 V, and the other cathodic peak is positioned at 0.60 V, which can be contributed by the reversible reduction of MnO_2 and Fe_3O_4 with lithium in the electrode, respectively. While the anodic peaks presenting at 1.21 V and 1.60 V can separately be assigned to the electrochemical oxidation reaction for MnO_2[27] and Fe_3O_4. Due to the polarization of active materials and the formation of SEI layer in the first cycle, all the cathodic and anodic peaks are shifted slightly toward to more positive potential, and the peak intensities decrease during the second cycle. It is worth noting that the CV curves overlap well during the 30th and 50th cycles (Fig. 4e). This result means that the electrochemical reaction is highly reversible.

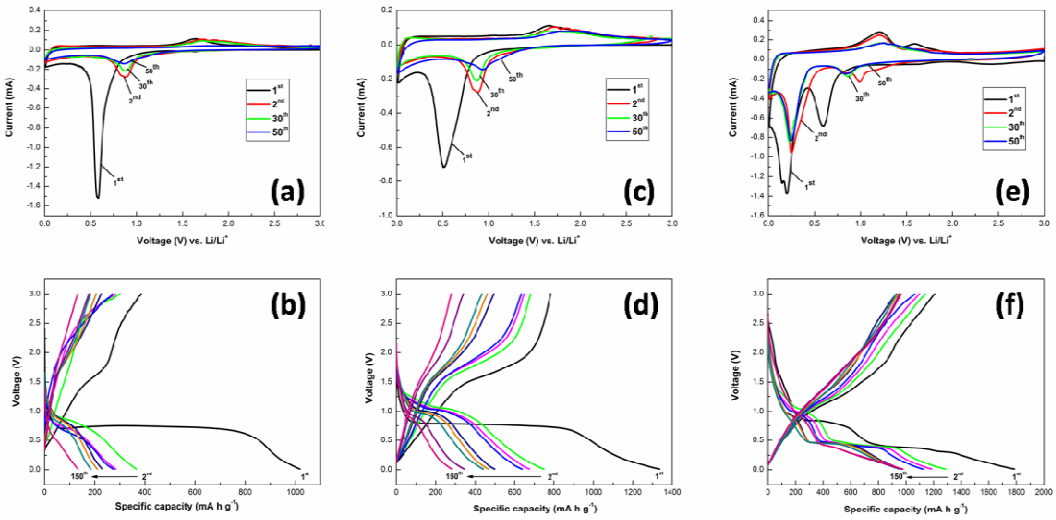

Fig. 5 CV curves and Charge-discharge profiles of (a and b) α-Fe_2O_3, (c and d) Fe_3O_4-C and (e and f) Fe_3O_4@(C-MnO_2) electrodes between 0.01 and 3 V at a scan rate of 0.1 mV s^{-1}.

The charge-discharge cycles for the prepared samples were tested within the cutoff voltage window of 0.01-3.0 V at a current density of 100 mA g^{-1} in coin-type lithium half cells, and the corresponding profiles are shown in Fig. 5(b, d and f). As

shown in Fig. 5b, the first discharge curve of α-Fe_2O_3 has an obvious potential plateau at about 0.8 V, which is similar to that reported for α-Fe_2O_3.[28, 29] It is evident that the discharge process of Fe_3O_4-C with an accordant voltage plateau of about 0.75 V manifests typical characteristics of Fe_3O_4 voltage trends for the anode.[30] In the case of the Fe_3O_4@(C-MnO_2), flat discharge plateaus at around 0.8 V and 0.45 V are observed in the first discharge cycle (Fig. 5f), correlating with the reduction process for Fe_3O_4 and MnO_2. The first specific discharge capacities for α-Fe_2O_3, Fe_3O_4-C and Fe_3O_4@(C-MnO_2) are 1018, 1336 and 1786 mA h g^{-1}, respectively. However, the discharge capacities for α-Fe_2O_3 and Fe_3O_4-C fade faster than Fe_3O_4@(C-MnO_2) during the subsequent cycles, only 385 and 782 mA h g^{-1} for the formers but 1300 mA h g^{-1} for Fe_3O_4@(C-MnO_2) in the second cycles. Thus, the bare α-Fe_2O_3 and Fe_3O_4-C show a remarkable irreversible capacity loss arising from the relatively large volume change during the lithiation/delithiation process and the decomposition of solvent in the electrolyte forming a solid electrolyte interphase (SEI).[31, 32] Besides, the discharge capacities of the α-Fe_2O_3 and Fe_3O_4-C drop rapidly to 118 and 294 mA h g^{-1}, respectively, in contrast, that of Fe_3O_4@(C-MnO_2) reduces slightly and still remains a high capacity of 979 mA h g^{-1} up to 150 cycles. Accordingly, the capacity and cycling stability of Fe_3O_4@(C-MnO_2) are significantly improved.

Fig. 6a compares the cycling performance of three samples at a current density of 100 mA g^{-1} in the voltage range of 0.01-3 V. Since the carbon layer can provide mechanical protection and stabilize the SEI layer at lower potential, the Fe_3O_4-C exhibits a better cycling performance than the pure α-Fe_2O_3, and the discharge

capacity of Fe_3O_4-C stabilizes at ~435 mA h g^{-1} whereas that of α-Fe_2O_3 is only ~141 mA h g^{-1}. Moreover, owing to the larger specific surface and high theoretical capacity of MnO_2 located on the surface of the Fe_3O_4-C, the specific discharge capacity of the Fe_3O_4@(C-MnO_2) can be greatly improved to ~970 mA h g^{-1}, which is over twofold of Fe_3O_4-C. Coulombic efficiency (CE) is an important parameter to evaluate electrochemical performance.[33, 34] The CEs of three samples are compared in Fig. 6c. It can be seen that the initial CE of the Fe_3O_4@(C-MnO_2) is ~70%, which is significantly higher than that of α-Fe_2O_3 (~42%) and Fe_3O_4-C (~60%). After several cycles, the CE of Fe_3O_4@(C-MnO_2) increased to about 99%, however, only ~97% and ~96% for α-Fe_2O_3 and Fe_3O_4-C, respectively. Therefore, it can be concluded that the combination of the carbon coating as well as the MnO_2 layer makes obviously contribution to the higher cycling performance, capacity and higher CE for the Fe_3O_4@(C-MnO_2). In particular, the high surface area and high theoretical capacity of MnO_2 could contribute to excellent capacity of Fe_3O_4@(C-MnO_2); besides, the loose MnO_2 layer could provide buffering space to accommodate the huge volume change of the active materials and prevent the aggregation of particles during cycles, thus improving the cycling performance of the composite. Interestingly, from the 80th cycle onward, the capacity of the Fe_3O_4@(C-MnO_2) increased gradually to a value as high as 979 mA h g^{-1} until 150 cycles. This phenomenon may probably be attributed to the reversible formation of organic polymeric/gel like films by decomposition at low potentials.[35, 36]

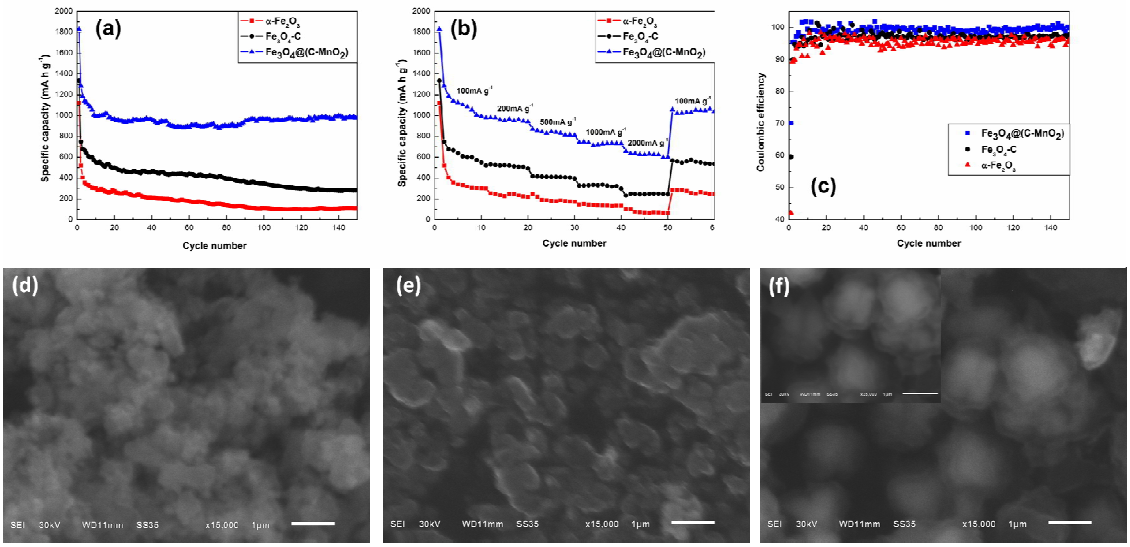

311

312 **Fig. 6** Cycling performance (a) of three samples at a current density of 100 mA g^{-1}; rate
313 performance (b) of three samples at various current densities from 100 to 2000 mA g^{-1}; coulombic
314 efficiencies (c) of three samples at 200 mA g^{-1} during the first 150 cycles; SEM images after 150
315 cycles at 100 mA g^{-1} for (d) α-Fe_2O_3, (e) Fe_3O_4-C and (f) Fe_3O_4@(C-MnO_2).

316 To investigate the effect of MnO_2 on the structure of Fe_3O_4@(C-MnO_2), SEM
317 after 150 cycles at 100 mA g^{-1} were taken for all three samples. As shown in Fig. 6f,
318 although the size of particle has a little increase after 150 cycles, the structure of
319 Fe_3O_4@(C-MnO_2) is retained well without agglomeration, which can be ascribed to
320 that the MnO_2 layer could buffer volume expansion and alleviate the structure damage
321 during cycling. On the contrary, as for α-Fe_2O_3 (Fig. 6d), without any protected layers,
322 it looks seriously aggregated and pulverized. In the meantime, Fig. 6e shows Fe_3O_4-C
323 particle is not collapsed as severe as α-Fe_2O_3 due to the protection of carbon layer. As
324 a result, the MnO_2 layer could well preserve the structural integrity of
325 Fe_3O_4@(C-MnO_2) during the long-term charge/discharge cycles.

326 Rate capability is also of great significant characteristic for high performance
327 LIBs. Fig. 6b illustrates the rate performance of α-Fe_2O_3, Fe_3O_4-C and

328 Fe_3O_4@(C-MnO_2) electrodes at various current densities from 100 to 2000 mA g^{-1} so
329 as to examine the effects of carbon and MnO_2 layers on rate capability. On account of
330 the superior electronic conductivity of carbon, the Fe_3O_4-C exhibits better rate
331 capability than the bare α-Fe_2O_3. The discharge capacities of ~650, ~410 and ~250
332 mA h g^{-1} for Fe_3O_4-C are much higher than ~400, ~200 and ~75 mA h g^{-1} for α-Fe_2O_3
333 under the current densities of 100, 500 and 2000 mA g^{-1}, respectively. In the case of
334 Fe_3O_4@(C-MnO_2), at a low current density of 100 mA g^{-1}, the discharge capacity is as
335 high as ~1100 mA h g^{-1}, especially, even as the current densities increasing to 500 and
336 2000 mA g^{-1}, it still delivers discharge capacities of ~860 and ~630 mA h g^{-1}
337 respectively. Compared with Fe_3O_4-C, it can be unambiguously seen that the
338 Fe_3O_4@(C-MnO_2) possesses a remarkably high capacity and improved rate
339 performance. When the current density is finally returned to its initial value of 100
340 mA g^{-1}, the discharge capacity of ~1040 mA h g^{-1} can still be observed for the
341 Fe_3O_4@(C-MnO_2) sample, but only ~545 and ~260 mA h g^{-1} for Fe_3O_4-C and α-Fe_2O_3,
342 which further verifies the merits of this core-double-shell structure. Consequently, it is
343 worth noting that the superior rate performance for Fe_3O_4@(C-MnO_2) is most likely
344 owing to not only high electronic conductivity of the carbon layer but also high
345 capacity combination of MnO_2 and Fe_3O_4.

346 To further understand the superior electrochemical performance of
347 Fe_3O_4@(C-MnO_2) as anode material, electrochemical impedance spectroscopy (EIS)
348 measurements of the three electrodes were carried out at around 2.5 V (room
349 temperature) on cells comprising the samples as the working electrode versus Li

before the discharge-charge cycles. As shown in Fig. 7a, the Nyquist plots of the three electrodes are similar to each other, with a semicircle at high-medium frequency and an inclined straight line at low frequency. It is well known that the high-frequency semicircle is related to the ohmic resistance of the cell from Z' axis interception and attributed to the contact resistance, polarization resistance, charge transfer resistance and corresponding capacitances interception; the oblique line in the low frequency range indicates the Warburg impedance (W_s), which is associated with lithium-ion diffusion through electrodes. The equivalent circuit model (in Fig. 7b) is used to fit the EIS data, where R_s is known as the ohmic resistance, and R_{ct} is the charge transfer resistance. Nyquist plots are fitted as the magenta curves (in Fig. 7a) and the fitted impedance data are listed in Table 1. As shown in Fig. 7a, the fitting patterns are well agreement with the experimental EIS data. It can be seen from Table 1 that the R_s data of three samples show slight difference. The R_s of Fe_3O_4@(C-MnO_2) (5.116 Ω) is slightly higher than that of the others owing to the low electronic conductivity of MnO_2. In addition, the R_{ct} value of Fe_3O_4@(C-MnO_2) (111.8 Ω) is less than that of α-Fe_2O_3 (373.1 Ω) and Fe_3O_4-C (231.1 Ω), indicating the lowest charge-transfer resistance of Fe_3O_4@(C-MnO_2) electrode. These results suggest that the Fe_3O_4@(C-MnO_2) electrode has the lowest activation energy for the Li^+ diffusion and undergoes a fast Faradaic reaction, confirming the significantly enhanced cycling performance and electrochemical dynamic behavior of Fe_3O_4@(C-MnO_2) anode in comparison to the other two electrodes.

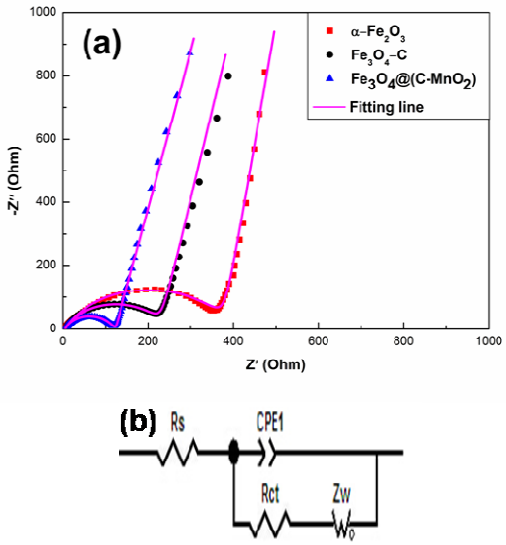

371

372 **Fig. 7** (a) The electrochemical impedance spectras (EIS) of α-Fe_2O_3, Fe_3O_4-C and

373 Fe_3O_4@(C-MnO_2) electrodes. (b) The equivalent circuit used for fitting the experimental EIS data.

374

375 **Table 1** R_s and R_{ct} values obtained from equivalent circuit fitting of experimental data for α-Fe_2O_3,

376 Fe_3O_4-C and Fe_3O_4@(C-MnO_2) electrodes.

samples	α-Fe_2O_3	Fe_3O_4-C	Fe_3O_4@(C-MnO_2)
R_s (Ω)	5.090	5.045	5.116
R_{ct} (Ω)	373.1	231.1	111.8

377

378 ## 4. Conclusions

379 In summary, we have successfully synthesized the unique Fe_3O_4@(C-MnO_2)

380 core-double-shell composite with cube-like morphology as an anode material for LIBs

381 by the hydrothermal method and LBL technique. The Fe_3O_4-C particle was prepared

382 via partial reduction of α-Fe_2O_3 cube with carbon coating in a calcination process; the

Fe_3O_4@(C-MnO_2) core-double-shell composite was further formed by following a mild hydrothermal redox reaction between $KMnO_4$ and Fe_3O_4-C. The Fe_3O_4@(C-MnO_2) composite exhibits the markedly improved electrochemical performance, including a higher discharge capacity of exceeding 1000 mA h g^{-1} at a current density of 100 mA g^{-1}, superior rate capability with the discharge capacity of ~630 mA h g^{-1} even as the current density increasing to 2000 mA g^{-1}, and excellent cycling stability with a capacity of 979 mA h g^{-1} after 150 cycles at the current density of 100 mA g^{-1}. These outstanding performances mainly can be attributed to the high theoretical capacity and larger specific surface of MnO_2. In addition, the MnO_2 nanomaterials deposited on the surface of Fe_3O_4-C materials are of benefit to further accommodate the large volume change and alleviated structure damage during battery cycling to some extent. Therefore, this novel Fe_3O_4@(C-MnO_2) core-double-shell architecture with cube-like morphology could be extended to other active TMOs, thus providing an innovative strategy for designing new anode materials of next-generation LIBs.

Acknowledgements

This work was financially supported by the National Natural Science Foundation of China (Grant Nos. 51072173, 51272221, 51302239 and 21203161), Specialized Research Fund for the Doctoral Program of Higher Education (Grant No. 20134301130001), the Natural Science Foundation of Hunan Province, China (Grant No. 13JJ4051).

References

1. J. Jiang, Y. Li, J. Liu, X. Huang, C. Yuan and X. W. Lou, *Adv. Mater.*, 2012, 24, 5166.

2. L. Ji, Z. Lin, M. Alcoutlabi and X. Zhao, *Energy Environ. Sci.*, 2011, 4, 2682.

3. P. G. Bruce, B. Scrosati and J. M. Tarascon, *Angew. Chem. Int. Ed.*, 2008, 47, 2930.

4. S. Mitra, P. Poizot, A. Finke and J. -M. Tarascon, *Adv. Funct. Mater.*, 2006, 16, 2281.

5. J. Zhu, Z. Yin, D. Yang, T. Sun, H. Yu, H.E. Hoster, H. H. Hng, H. Zhang and Q. Yan, *Energy Environ. Sci.*, 2013, 6, 987.

6. H. Wang, J. Liu, X. Wang, C. Wu, Q. Zhao, Q. Fu, X. Yang and H. Shu, *RSC Adv.*, 2014, 4, 22241.

7. D. Su, S. Dou and G. Wang, *Nano Res.*, 2014, 7, 794.

8. Y. Zhu, H, Guo, Y. Wu, C. Cao, S. Tao and Z. Wu, *J. Mater. Chem. A*, 2014, 2, 7904.

9. Y. Chen, B. Song, X. Tang, L. Lu and J. Xue, *J. Mater. Chem.*, 2012, 22, 5006.

10. T, Muraliganth, A. V. Murugan and A. Manthiram, *Chem. Commun.*, 2009, 7360.

11. L. Lang and Z. Xu, *ACS Appl. Mater. Interfaces*, 2013, 5, 1698.

12. L. Bo, H. Cao, J. Shao and M. Qu, *Chem. Commun.*, 2011, 47, 10374.

13. L.J. Fu, H. Liu, H.P. Zhang, C. Li, T. Zhang, Y.P. Wu, R. Holze and H.Q. Wu, *Electrochem. Commum.*, 2006, 8, 1.

14. W.M. Zhang, X.L. Wu, J.S. Hu, Y.G. Guo and L.J. Wang, *Adv. Funct. Mater.*, 2008, 18, 3941.

15. Q.Q. Xiong, Y. Lu, X.L. Wang, C.D. Gu, Y.Q. Qiao and J.P. Tu, *J. Alloys Compd.*,

2012, 536, 219.

16. J. Liu, J. Ni, Y. Zhao, H. Wang and L. Gao, *J. Mater. Chem. A*, 2013, 1, 12879.

17. Z. X. Yang, G. D. Du, Q. Meng, Z. P. Guo, X. B. Yu, Z. X. Chen, T. L. Guo, R. Zeng, *RSC Adv.*, 2011, 1, 1834-1840.

18. Y. Luo, J. Luo, J. Jiang, W. Zhou, H. Yang, X. Qi, H. Zhang, H. J. Fan, D. Y. W. Yu, C. M. Li and T. Yu, *Energy Environ. Sci.*, 2012, 5, 6559.

19. D. Su, H. -J. Ahn and G. Wang, *J. Mater. Chem. A*, 2013, 1, 4845.

20. T.X. T. Sayle, R. R. Maphanga, P.E. Ngoepe and D.C. Sayle, *J. Am. Chem. Soc.*, 2009, 131, 6161.

21. A. L. M. Reddy, M.M. Shaijumon, S.R. Gowda and P.M. Ajayan, *Nano Lett.*, 2009, 9, 1002.

22. H. Xia, M. Lai and L. Lu, *J. Mater. Chem.*, 2010, 20, 6896.

23. J.Y. Liao, D. Higgins, G. Lui, V. Chabot, X. Xiao and Z. Chen, *Nano Lett.*, 2013, 13, 5467.

24. D. Larcher, D. Bonnin, R. Cortes, L. Rivals, L. Personnaz and J. -M. Tarascon, *J. Electrochem. Soc.*, 2003, 150, A1643.

25. P. Wang, M. Gao, H. Pan, J. Zhang, C. Liang, J. Wang, P. Zhou and Y. Liu, *J. Power Sources*, 2013, 239, 466.

26. Y. NuLi, P. Zhang, Z. Guo, P. Munroe and H. Liu, *Electrochim. Acta.*, 2008, 53, 4213.

27. M.S. Wu and P.C. J. Chiang, *Electrochem. Commum.*, 2006, 8, 383.

28. H. Xiao, Y. Xia, W. Zhang, H. Huang, Y. Gan and X. Tao, *J. Mater. Chem. A*, 2013,

1, 2307.

29. A. Brandt and A. Balducci, *J. Power Sources*, 2012, 230, 44.

30. X. Li, X. Huang, D. Liu, X. Wang, S. Song, L. Zhou and H. Zhang, *J. Phys. Chem. C*, 2011, 115, 21567.

31. S. Laruelle, S. Grugeon, P. Poizot, M. Dollé, L. Dupont and J. -M. Tarascon, *J. Electrochem. Soc.*, 2002, 149, A627.

32. Y. Wang, F. Su, J. Y. Lee and X. S. Zhao, *Chem. Mater.*, 2006, 18, 1347.

33. T. M. Bond, J. C. Burus, D. A. Stevens, H. M. Dahn and J. R. Dahn, *J. Electrochem. Soc.*, 2013, 160, A521.

34. A. J. Smith, J. C. Burus, J. R. Dahn, *Electrochem. Solid-State Lett.*, 2010, 13, A177.

35. S. -W. Kim, D. -H. Seo, H. Gwon, J. Kim and K. Kang, *Adv. Mater.*, 2010, 22, 5260.

36. Y. Hou, Y. Cheng, T. Hobson and J. Liu, *Nano Lett.*, 2010, 10, 2727.